



Article

# Large-Scale Screening and Machine Learning for Metal–Organic Framework Membranes to Capture CO<sub>2</sub> from Flue Gas

Yizhen Situ<sup>1</sup>, Xueying Yuan<sup>1</sup>, Xiangning Bai<sup>1</sup>, Shuhua Li<sup>1</sup>, Hong Liang<sup>1</sup>, Xin Zhu<sup>1,\*</sup>, Bangfen Wang<sup>1,\*</sup>  
and Zhiwei Qiao<sup>1,2,\*</sup>

- <sup>1</sup> Guangzhou Key Laboratory for New Energy and Green Catalysis, School of Chemistry and Chemical Engineering, Guangzhou University, Guangzhou 510006, China; 2112005038@e.gzhu.edu.cn (Y.S.); 2111905092@e.gzhu.edu.cn (X.Y.); baixiangning@e.gzhu.edu.cn (X.B.); lish@gzhu.edu.cn (S.L.); lhong@gzhu.edu.cn (H.L.)
- <sup>2</sup> Joint Institute of Guangzhou University & Institute of Corrosion Science and Technology, Guangzhou University, Guangzhou 510006, China
- \* Correspondence: zhux@gzhu.edu.cn (X.Z.); bwang@gzhu.edu.cn (B.W.); zqiao@gzhu.edu.cn (Z.Q.)

**Abstract:** To combat global warming, as an energy-saving technology, membrane separation can be applied to capture CO<sub>2</sub> from flue gas. Metal–organic frameworks (MOFs) with characteristics like high porosity have great potential as membrane materials for gas mixture separation. In this work, through a combination of grand canonical Monte Carlo and molecular dynamics simulations, the permeability of three gases (CO<sub>2</sub>, N<sub>2</sub>, and O<sub>2</sub>) was calculated and estimated in 6013 computation-ready experimental MOF membranes (CoRE–MOFMs). Then, the relationship between structural descriptors and permeance performance, and the importance of available permeance area to permeance performance of gas molecules with smaller kinetic diameters were found by univariate analysis. Furthermore, comparing the prediction accuracy of seven classification machine learning algorithms, XGBoost was selected to analyze the order of importance of six structural descriptors to permeance performance, through which the conclusion of the univariate analysis was demonstrated one more time. Finally, seven promising CoRE–MOFMs were selected, and their structural characteristics were analyzed. This work provides explicit directions and powerful guidelines to experimenters to accelerate the research on membrane separation for the purification of flue gas.

**Keywords:** membrane separation; metal–organic frameworks; machine learning



**Citation:** Situ, Y.; Yuan, X.; Bai, X.; Li, S.; Liang, H.; Zhu, X.; Wang, B.; Qiao, Z. Large-Scale Screening and Machine Learning for Metal–Organic Framework Membranes to Capture CO<sub>2</sub> from Flue Gas. *Membranes* **2022**, *12*, 700. <https://doi.org/10.3390/membranes12070700>

Academic Editor: Jason Bara

Received: 28 June 2022

Accepted: 8 July 2022

Published: 11 July 2022

**Publisher's Note:** MDPI stays neutral with regard to jurisdictional claims in published maps and institutional affiliations.



**Copyright:** © 2022 by the authors. Licensee MDPI, Basel, Switzerland. This article is an open access article distributed under the terms and conditions of the Creative Commons Attribution (CC BY) license (<https://creativecommons.org/licenses/by/4.0/>).

## 1. Introduction

With the rapid development of industry, global warming has increased, with increasing emissions of CO<sub>2</sub>, which is very harmful to the life and development of humans [1]. Because it is impossible to completely develop industry without carbon in a short time, the capture of CO<sub>2</sub> has become an essential way to reduce greenhouse gas emissions and improve the present condition. However, CO<sub>2</sub> capture is an energy-intensive process for a series of reasons, among which is the gas composition [1]. Therefore, it is an urgent need to develop energy-saving technology to separate CO<sub>2</sub> from gas mixtures. Comparing with a series of separation technologies, membrane separation has received much attention due to its efficiency, low-energy consumption, and requirement of relatively simple equipment [2]. However, the search is on for a membrane that shows good separation performance with wide application, especially when complex components are involved. The development of materials with good membrane separation performance has become a hot topic in recent years.

In the last twenty years, new materials metal–organic frameworks (MOFs), self-assembled by a wide range of organic links and metal nodes, have been considered to have

potential for use in domains such as drug delivery [3], catalysis [4], gas storage [5–7], gas adsorption and separation [8–12] due to their excellent characteristics such as large surface area and high porosity. Commonly, MOFs can be applied as adsorbates and membranes for the separation of gas mixtures. For example, designing porous materials at the molecular level for adsorption-based application, PCN-88 was synthesized by Li et al. [13] based on a new concept, ‘single-molecule trap’, which showed excellent preferential adsorption of CO<sub>2</sub> over N<sub>2</sub> and CH<sub>4</sub>. With two new empirical equations for the prediction of hydrogen adsorption capacity by pore volume by Zhang et al. [14], NPF-200 was predicted and demonstrated as a promising MOF for H<sub>2</sub> storage. Further, an MOF, CAU-10-NH<sub>2</sub>, with excellent water stability/reusability was synthesized by their team [15], regarded as a promising material for C<sub>2</sub>H<sub>2</sub>/CO<sub>2</sub> separation. Boyd et al. [16] synthesized two MOFs containing the most hydrophobic adsorbaphore found by the evaluation of the CO<sub>2</sub>/N<sub>2</sub> selectivity of MOFs in wet flue gas through computational screening. They found that both of their CO<sub>2</sub>/N<sub>2</sub> separation performances were not affected by water. Nugent et al. [17] demonstrated the feasibility of a crystal engineering or reticular chemistry strategy, which controls pore functionality and size for the improvement of CO<sub>2</sub> separation performance, through the synthesis of SIFSIX-2-Cu, SIFSIX-2-Cu-i, and SIFSIX-3-Zn. Although adsorption technology can be used to separate gas mixtures, membrane separation is an attractive option for its lower energy consumption [2]. In the field of membrane separation, MOF membranes (MOFMs) have been demonstrated as a kind of material with great potential to separate gas mixtures [2]. For example, Yin et al. [18] synthesized a thin tubular CAU-1 membrane exhibiting a high permeance of up to  $1.34 \times 10^{-6} \text{ mol}\cdot\text{m}^{-2}\cdot\text{s}^{-1}\cdot\text{Pa}^{-1}$  for CO<sub>2</sub> and excellent selectivity of 17.4–22.8 for CO<sub>2</sub>/N<sub>2</sub> mixture. Chang et al. [19] found that with the coating of a Pebax<sup>®</sup>1657 layer on the surface, the H<sub>2</sub>/CO<sub>2</sub> separation performance of a ZIF-7-NH<sub>2</sub> membrane can be improved. Kang et al. [20] found that the 1,2-bis-(4-pyridyl) ethylene (BPE) molecule distributed in channels can improve the H<sub>2</sub>/CO<sub>2</sub> separation performance of the [Ni<sub>2</sub>(L-asp)<sub>2</sub>(BPE)]·(G) membrane. Under a two-step coating process, a new MOF-based membrane (PAN-γ-CD-MOF-PU membrane) was fabricated by Fan et al. [21], with a permeability to CO<sub>2</sub> of over 70 barrer and selectivity to CO<sub>2</sub>/N<sub>2</sub> and CO<sub>2</sub>/O<sub>2</sub> of 253.46 and 154.28, respectively. Yan et al. [22] synthesized a UiO-66 membrane through tertiary growth at room temperature, which exhibited an optimal selectivity of 37.8 for CO<sub>2</sub>/N<sub>2</sub>. Chen et al. [23] fabricated a ZIF-8 membrane under different reaction conditions, and found that the optimal temperature for synthesis of ZIF-8 membrane is 80 °C. Further, they also found that the separation factor of CO<sub>2</sub>/N<sub>2</sub> was 5.49 and the permeance of CO<sub>2</sub> was  $0.47 \times 10^{-7} \text{ mol}\cdot\text{m}^{-2}\cdot\text{s}^{-1}\cdot\text{Pa}^{-1}$  under optimal conditions. However, with the increasing number of MOFs synthesized by experiments and built by computer technology, it is not practical to select potential MOFMs only through experiments due to the high costs and long time periods involved. Further, a series of chemical reagents are harmful to experimenters and the environment. There is an urgent need to develop a rapid method to select MOFMs with excellent performance.

Recently, high-throughput computational screening based on molecular simulation technology has been demonstrated as a useful way to accelerate the research on MOFMs by previous studies. For example, Qiao et al. [24] calculated the performance of 137,953 MOFMs by grand canonical Monte Carlo (GCMC) and molecular dynamics (MD) simulations and finally screened 24 optimal MOFMs for CO<sub>2</sub>/N<sub>2</sub>/CH<sub>4</sub> separation. Applying GCMC and equilibrium MD simulations, Glover et al. [25] studied the separation performance of MOFMs for CO<sub>2</sub>/CH<sub>4</sub> and H<sub>2</sub>S/CH<sub>4</sub>. They screened eight top-performing MOFMs superior than polymer membranes, zeolite membranes, and mixed matrix membranes (MMMs). Azar et al. [26] analyzed the H<sub>2</sub>/N<sub>2</sub> separation performance of more than 3000 different types of MOF membranes and examined their separation potential in MMMs by molecular simulation. They found the characteristics of most promising MOFMs and the great advantage of incorporating MOFs into polymers. In the same way, Daglar et al. [27] screened optimal membranes for CO<sub>2</sub>/N<sub>2</sub>/H<sub>2</sub>O separation and explored the structure–performance relationship. They found that MOFMs with narrow pores, low surface areas, and mono-

clinic and lanthanide-containing structures are the best candidates for CO<sub>2</sub>/N<sub>2</sub> membrane separation. Altintas et al. [28] used molecular simulation to explore the relationship between 175 different structures of MOFMs and the separation performance of C<sub>2</sub>H<sub>6</sub>/C<sub>2</sub>H<sub>4</sub> and C<sub>2</sub>H<sub>6</sub>/CH<sub>4</sub>. They found that MOFMs with high C<sub>2</sub>H<sub>6</sub> selectivity are those with cavity diameters between 6 and 9 Å, porosities lower than 0.5 and surface areas between 500 and 1000 m<sup>2</sup>g<sup>-1</sup>. Wang et al. [29] studied H<sub>2</sub>/CH<sub>4</sub> separation using an IRMOF-1 membrane through a dual-force zone nonequilibrium molecular dynamics simulation. They reached the conclusion that both structural and chemical features of functionalized MOFMs determine gas separation performance. Bai et al. [30] screened MOFMs for the separation of gas pairs including H<sub>2</sub> by molecular simulation and machine learning, and found 15 MOFMs with excellent separation performance.

Commonly, there are several compositions of industrial flue gas in addition to CO<sub>2</sub>, such as N<sub>2</sub> and O<sub>2</sub> [31–33]. In this work, the volume ratio of CO<sub>2</sub>, N<sub>2</sub>, and O<sub>2</sub> is considered as 1:1:1. For the screening of MOFMs with great potential for ternary CO<sub>2</sub>/N<sub>2</sub>/O<sub>2</sub> separation, the permeability (*P*) of pure CO<sub>2</sub>, N<sub>2</sub>, and O<sub>2</sub> in MOFMs was calculated by GCMC and MD simulations. Then, through univariate analysis and machine learning, the relationship between structural descriptors and permeance performance was explored. Finally, seven promising MOFMs for ternary gas pair separation were screened.

## 2. Methods

### 2.1. Model

MOFMs studied in this work were MOFs from the 2019 computation-ready experimental metal-organic frameworks (CoRE-MOFs) database [34]. The structural parameters of CoRE-MOFs were derived from experimental data after free solvent molecules were removed [34,35]. The atomic structure of MOFs was described by Lennard-Jones (LJ) parameters and electrostatic potentials

$$u_{\text{LJ+elec}}(r) = \sum 4\varepsilon_{ij} \left[ \left( \frac{\sigma_{ij}}{r_{ij}} \right)^{12} - \left( \frac{\sigma_{ij}}{r_{ij}} \right)^6 \right] + \sum \frac{q_i q_j}{4\pi\varepsilon_0 r_{ij}} \quad (1)$$

where  $\varepsilon_{ij}$  is the potential energy parameter,  $\sigma_{ij}$  represents the equilibrium distance between atoms, and  $r_{ij}$  is the distance between atom pairs.  $q_i$ ,  $q_j$  is the atomic charge of atoms  $i$  and atoms  $j$ ,  $\varepsilon_0 = 8.8542 \times 10^{-12} \text{ C}^2 \cdot \text{N}^{-1}$ , which represents the permittivity of vacuum. The atomic charge of MOFs was quickly calculated by the MEPO-Qeq method [36]. All LJ potential energy parameters of MOFs are listed in Table S1, and they come from universal force field (UFF) [37]. The structural characteristics of MOFs are represented by six descriptors, in which the volumetric surface area (VSA) and fraction ( $\phi$ ) were calculated using N<sub>2</sub> with a diameter of 3.64 Å and He with a diameter of 2.58 Å as a probe using the RASPA software package, and both the pore limited diameter (PLD) and largest cavity diameter (LCD) were estimated by the Zeo++ software package [38,39].

For CO<sub>2</sub>, O<sub>2</sub>, and N<sub>2</sub> molecules, force field parameters were adopted from the transferable potentials for phase equilibria (TraPPE) force field [40], listed in Table S2. For CO<sub>2</sub>, the bond length of C–O is 1.16 Å, and the bond angle ∠OCO is 180°. For N<sub>2</sub>, which is considered as a three-site model, the N–N bond length is 1.10 Å. O<sub>2</sub> is a three-site atom. A large number of studies have demonstrated that the application of UFF for MOFs and TraPPE for gases can accurately predict the gas adsorption and diffusion in various MOFs [41–44].

### 2.2. Molecular Simulation

In this work, the adsorption, diffusion, and permeability behaviors of pure CO<sub>2</sub>, O<sub>2</sub>, and N<sub>2</sub> in MOFMs were simulated by GCMC and MD. Each GCMC or MD simulation was independently carried out and the interaction between MOFs and adsorbate molecules was calculated by the Lorentz–Berthelot rule. The periodic boundaries were applied in the three-dimensional system and the unit cell of each MOF was expanded to at least 24 Å in all the dimensions. To calculate LJ interactions, the spherical cutoff was set to 12 Å for

long-range correction, and the framework–gas and gas–gas electrostatic interactions were calculated by Ewald summation [45]. Each GCMC simulation was run for 10,000 cycles, with the first 5000 cycles for the equilibration of simulation system and the last 5000 cycles for ensemble averages. Each cycle consisted of  $n$  trial moves ( $n$ : the number of adsorbate molecules), including translation, rotation, regrowth, and swap (insertion and deletion). The final simulation state of GCMC was used as the initial simulation state of MD. The MD duration in each MOF was 7 ns with the last 5 ns for production. All simulations of GCMC and MD were run under the RASPA software package [38]. After GCMC and MD simulations of each MOFM, the permeability of pure gases was calculated by

$$P_i = K_i \times D_i \quad (2)$$

where  $D_i$  is the diffusivity of component  $i$  in MOFMs, and  $K_i$  is Henry's constant of component  $i$ .

### 2.3. Evaluation of the Performance of MOFMs

Normally, evaluation of the performance of MOFMs includes gas permeance performance and gas diffusion performance. To select a series of MOFMs to separate ternary gas pairs, the separation performance of MOFMs for two binary gas pairs was firstly analyzed considering the complexity of ternary gas pairs. In this work, considering the adsorption–diffusion mechanism in the process of porous membrane separation, adsorption selectivity ( $S_{ads}$ ) has also been considered, which was calculated by

$$S_{ads(i/j)} = K_i/K_j \quad (3)$$

Meanwhile, gas diffusion performance was evaluated by the  $D_i$  and diffusion selectivity ( $S_{diff}$ ), where  $S_{diff}$  was calculated by

$$S_{diff(i/j)} = D_i/D_j \quad (4)$$

and gas permeance performance was evaluated by  $P_i$  and permselectivity ( $S_{perm}$ ), where  $S_{perm}$  was calculated by

$$S_{perm(i/j)} = P_i/P_j = S_{diff(i/j)} S_{ads(i/j)} \quad (5)$$

### 2.4. Machine Learning

To comprehensively analyze the relationship between structural descriptors and the permeance performance of MOFMs, seven classification machine learning algorithms were used to predict categories of MOFMs and calculate the relative importance (RI) of structural descriptors, which are support vector machine (SVM),  $k$ -nearest neighbor (KNN), decision tree (DT), random forest (RF), gradient boosting decision tree (GBDT), light gradient boosting machine (LGBM), and extreme gradient boosting (XGBoost).

At this stage, two categories were divided from the middle based on the permeance performance of MOFMs. Further, six structural descriptors (LCD, PLD, VSA,  $\phi$ , the density ( $\rho$ ), and the pore size distribution percentage between 2.5 and 3.5 Å (PSD%<sub>(2.5–3.5)</sub>)) were applied, in which PSD%<sub>(2.5–3.5)</sub> was calculated by

$$\text{PSD}\%_{(d_1-d_2)} = A_{12}/A_{\text{total}} \times 100\% \quad (6)$$

where  $A_{\text{total}}$  is the area under the entire PSD curve for a given MOF and  $A_{12}$  is the area between two pore sizes,  $d_1$  and  $d_2$ . With a larger PSD%, there is a more significant proportion of uniform pores.

With five permeance performances of three components, in order to obtain a uniform calculation method for RI, after simply comparing the prediction accuracy of the algorithm, the optimal algorithm was selected. Then, after comparing the accuracy and stability of the optimal algorithm in detail with  $k$ -fold cross validation ( $k = 5, 10, \text{ and } 15$ ) five times,

the best model with the best number fold cross validation was selected to calculate the RI of structural descriptors. In our work, the prediction accuracy of the machine learning model is evaluated by the accuracy (A), the sensitive (SEN), and the specificity (SPC). More detailed descriptions of the above algorithms are presented as Supplementary Materials.

### 3. Results and Discussion

#### 3.1. Univariate Analysis

To efficiently screen top-performing MOFMs to separate ternary gas pairs, CO<sub>2</sub>/N<sub>2</sub>/O<sub>2</sub>, the relationship between the structural descriptors and permeance performance was analyzed. In Figures 1a and 2a, with the increase in VSA, PLD, LCD, and  $\phi$ ,  $P_{CO_2}$  increased rapidly when they were low and finally plateaued. However, the relationship between  $\rho$  and  $P_{CO_2}$  was contrary. With a larger  $\rho$ ,  $P_{CO_2}$  become smaller. A similar tendency can also be found for N<sub>2</sub> and O<sub>2</sub> in Figures S1a,b and S2c,d. In Figure 1b, Figure 2a,b, Figures S1c and S2a,b, for  $S_{perm} (CO_2/O_2)$  and  $S_{perm} (CO_2/N_2)$ , most of them were both large when VSA, PLD, LCD, and  $\phi$  were small, which decreased dramatically at first and then plateaued with the increase in VSA, PLD, LCD, and  $\phi$ . The above phenomenon can be attributed to the size of available permeance area. Usually, gas molecules with smaller kinetic diameters can permeate through MOFMs even if the pore size of MOFMs is small. However, with a larger pore size, gas molecules with larger kinetic diameters can also spread through MOFMs if the pore size is large enough. For VSA, with a larger VSA, the available permeance area for gas molecules becomes larger. This indicates that the permeance performance of gas molecules with smaller kinetic diameters places a greater demand on the channel and geometry area of MOFMs.

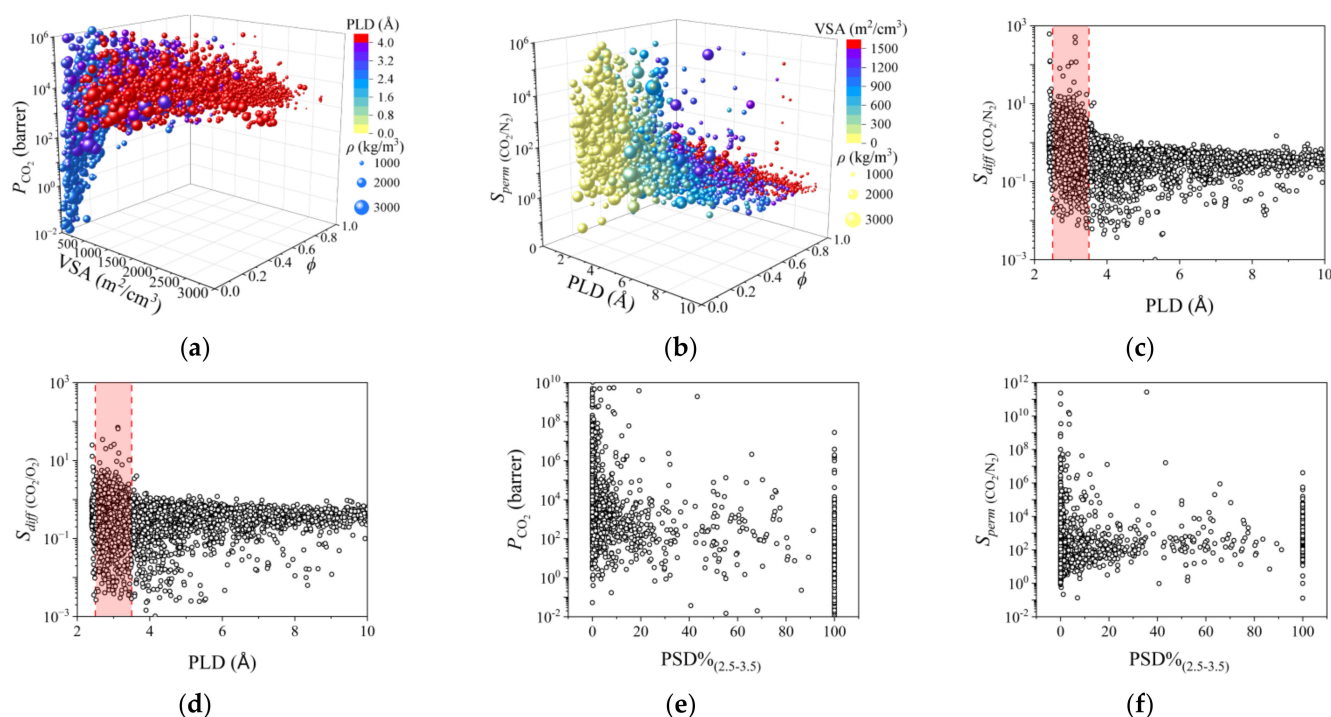


**Figure 1.** Structures–performance relationship studied by univariate analysis. (a)  $P_{CO_2}$ –VSA,  $\phi$ , PLD, and  $\rho$ ; (b)  $S_{perm} (CO_2/N_2)$ –VSA,  $\phi$ , PLD, and  $\rho$ ; (c)  $S_{diff} (CO_2/N_2)$ –PLD; (d)  $S_{diff} (CO_2/O_2)$ –PLD; (e)  $P_{CO_2}$ –PSD%<sub>0(2.5-3.5)</sub>; (f)  $S_{perm} (CO_2/N_2)$ –PSD%<sub>0(2.5-3.5)</sub>. In (a), the colors of balls represent PLD and the sizes of ball represent  $\rho$  of MOFMs. In (b), the colors of balls represent the VSA and the sizes of ball represent  $\rho$  of MOFMs.

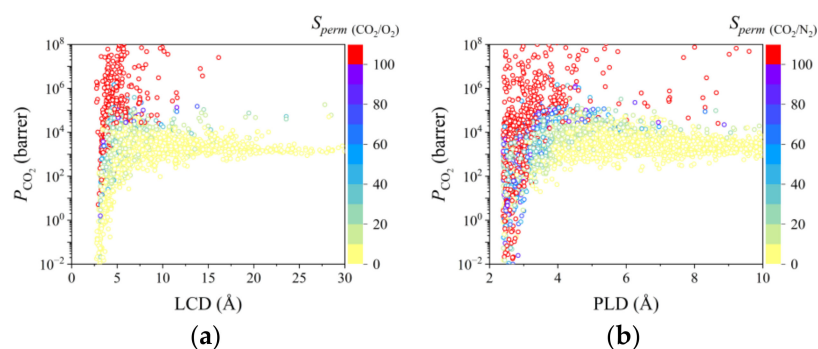


**Figure 2.** Relationship between LCD/PLD and permeance performance. (a) LCD– $P_{\text{CO}_2}$ – $S_{\text{perm}}(\text{CO}_2/\text{O}_2)$ ; (b) PLD– $P_{\text{CO}_2}$ – $S_{\text{perm}}(\text{CO}_2/\text{N}_2)$ .

Normally, the permeance performance of MOFMs is comprehensively decided by their adsorption and diffusion performance. Specially, diffusion performance is significantly related to PLD of MOFMs. So the relationship between diffusion performance and PLD was studied. In Figure S2e,  $D_{\text{N}_2}$  and  $D_{\text{O}_2}$  are similar, which is attributed to their similar kinetic diameter. Surprisingly, for  $\text{CO}_2$ , with the smallest kinetic diameter in three gas molecules,  $D_{\text{CO}_2}$  is smaller than  $D_{\text{N}_2}$  and  $D_{\text{O}_2}$ . This is because there are not only kinetic diameters but also other gas molecule properties impacting gas molecule diffusion. A similar phenomenon has also been found in previous research [24]. In Figure S2e, with the increase in PLD,  $D$  increases at first and then plateaus when PLD is larger than approximately 4 Å. For  $S_{\text{diff}}$ , with a larger PLD,  $S_{\text{diff}}$  shows a similar trend with  $S_{\text{perm}}$ . For two binary gas pairs, PLD ranges from approximately 2.5 to 3.5 Å, and  $P_{\text{CO}_2}$  and  $S_{\text{diff}}$  are both the largest. For better analysis of the relationship between structure and permeance performance, PSD%<sub>(2.5–3.5)</sub> was used for the further study. However, a decreasing trend was found in Figure 1e,f and Figure S3.

To better understand the separation mechanism, the relationship between  $P$ ,  $S_{\text{perm}}$ , and  $S_{\text{ads}}/S_{\text{diff}}$  was analyzed. In Figure 3a, the permeance performance of a large number of MOFMs for  $\text{CO}_2/\text{N}_2$  separation was found to exceed the 2008 Robeson upper bound [46]. Further, it is easy to find that with the increase in  $P_{\text{CO}_2}$ ,  $S_{\text{perm}}(\text{CO}_2/\text{O}_2)$  increases, as shown in Figure 3b. The above phenomenon indicates that there is a great possibility of finding a series of MOFMs for ternary gas pair separation. Moreover, the  $S_{\text{ads}}/S_{\text{diff}}$  becomes larger when  $P_{\text{CO}_2}$  and  $S_{\text{perm}}$  increase, which indicates that it is the adsorption mechanism and not the diffusion mechanism that plays a dominant role in membrane separation for  $\text{CO}_2/\text{N}_2$  and  $\text{CO}_2/\text{O}_2$  separation. This is attributed to the large quadrupole moment of  $\text{CO}_2$  impacting adsorption performance, which has been demonstrated previously [47–50].

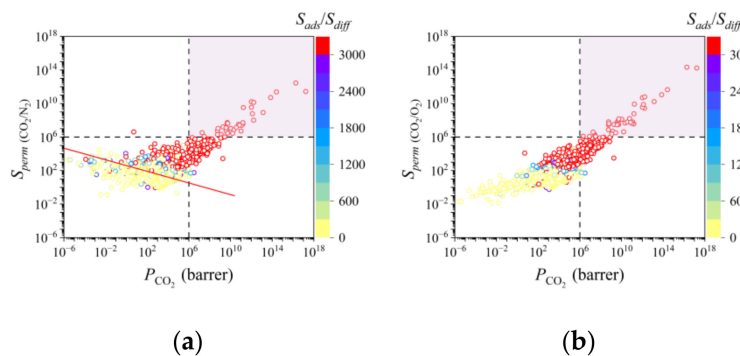


**Figure 3.** Relationship between  $P$ ,  $S_{\text{perm}}$ , and  $S_{\text{ads}}/S_{\text{diff}}$ . (a)  $P_{\text{CO}_2}$ – $S_{\text{perm}}(\text{CO}_2/\text{N}_2)$ – $S_{\text{ads}}(\text{CO}_2/\text{N}_2)/S_{\text{diff}}(\text{CO}_2/\text{N}_2)$ ; (b)  $P_{\text{CO}_2}$ – $S_{\text{perm}}(\text{CO}_2/\text{O}_2)$ – $S_{\text{ads}}(\text{CO}_2/\text{O}_2)/S_{\text{diff}}(\text{CO}_2/\text{O}_2)$ . In (a), the red line represents the 2008 Robeson upper bound.

### 3.2. Machine Learning

To comprehensively understand the order of impact importance of structural descriptors to the permeance performance of MOFMs, seven ML classification algorithms (SVM, KNN, DT, RF, GBDT, LGBM, and XGBoost) were applied to predict categories of MOFMs. Based on the performance of MOFMs, two categories were divided from the middle at first, in which  $P_1$  represents MOFMs with worse performance and  $P_2$  represents MOFMs with better performance. After comparison, XGBoost with optimal prediction performance was selected to predict categories of permeance performance.

From ML research, a series of conclusions were reached. (1) For  $P_{CO_2}$ , XGBoost with 10-fold cross validation showed the best prediction. In Figure 4c, there was an accuracy of 81% in general, and an accuracy of 81% for  $P_1$  and 82% for  $P_2$  in the confusion matrix. According to ML calculation, the order of RI is  $LCD > \phi > PLD > \rho > VSA > PSD\%_{(2.5-3.5)}$ . (2) For  $P_{O_2}$  and  $P_{N_2}$ , the best prediction was by XGBoost with 15-fold cross validation. In Figure S14a,b, there was an accuracy of 90% in general for  $P_{O_2}$  and there was an accuracy of 91% in general for  $P_{N_2}$ . In Figure 4e, the order of RI for  $P_{O_2}$  and  $P_{N_2}$  is similar—the order for  $P_{O_2}$  is  $\phi > PLD > LCD > VSA > \rho > PSD\%_{(2.5-3.5)}$  and for  $P_{N_2}$  is  $PLD > \phi > LCD > VSA > \rho > PSD\%_{(2.5-3.5)}$ . (3) For  $S_{perm} (CO_2/O_2)$  and  $S_{perm} (CO_2/N_2)$ , optimal prediction was by XGBoost with 10-fold and 5-fold cross validation. From ML calculation, the order of RI is shown in Figure 4f. For  $S_{perm} (CO_2/O_2)$ , the order of RI is  $LCD > VSA > PLD > \phi > \rho > PSD\%_{(2.5-3.5)}$ ; while, for  $S_{perm} (CO_2/N_2)$ , the order of RI is  $PLD > VSA > \phi > \rho > LCD > PSD\%_{(2.5-3.5)}$ .

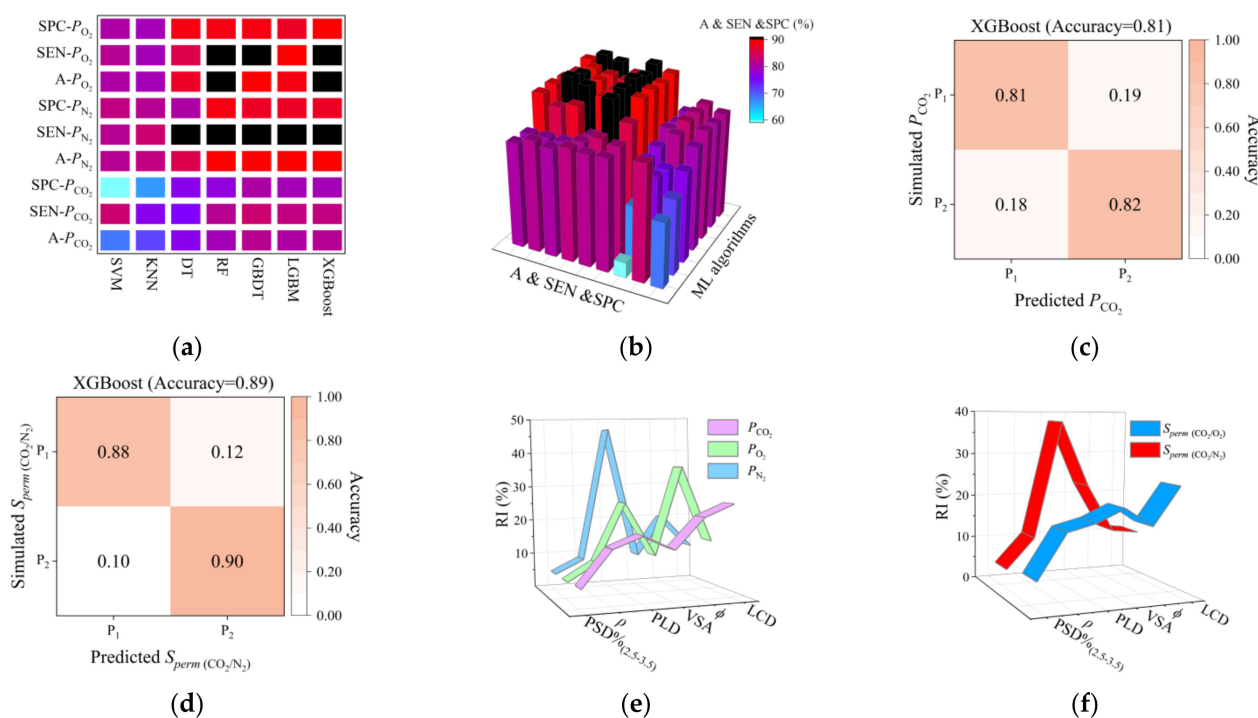


**Figure 4.** (a,b) Prediction accuracy comparison of seven classification algorithms; (c) confusion matrix for  $P_{CO_2}$ ; (d) confusion matrix for  $S_{perm} (CO_2/N_2)$ ; (e) RI comparison of  $P_{CO_2}$ ,  $P_{O_2}$ , and  $P_{N_2}$ ; (f) RI comparison of  $S_{perm} (CO_2/N_2)$  and  $S_{perm} (CO_2/O_2)$ .

Based on the above conclusions from ML, we found that of six structural descriptors, LCD, PLD, and  $\phi$  have a greater impact on gas molecule permeability. Further, the order of RI for LCD, VSA, and  $\rho$  for the permeability of three gas molecules is contrary to the order of RI of kinetic diameter. For  $S_{perm}$ , the order of RI of LCD and  $\rho$  for  $S_{perm} (CO_2/O_2)$  is larger than  $S_{perm} (CO_2/N_2)$ . Both confirm the conclusion by the univariate analysis that the permeance performance of gas molecules with smaller kinetic diameters places a greater demand on the channel and geometry area of MOFMs. On the contrary, the order of

RI of PLD for the permeability of three gas molecules is the same as the order of RI of kinetic diameter ( $Dia$ ),  $Dia_{N_2} > Dia_{O_2} > Dia_{CO_2}$ , because PLD plays an important role in the confirmation of diffusion barrier and determines the gas molecule diffusion barrier in porous materials [51,52]. This is also explained by the phenomenon that the importance of PLD to  $S_{perm}(CO_2/N_2)$  is larger than  $S_{perm}(CO_2/O_2)$ .

To better apply the ML result, the relationships between LCD and  $S_{perm}(CO_2/O_2)$  and between PLD and  $S_{perm}(CO_2/N_2)$  were analyzed in detail. From Figure 2a,b, the optimal LCD range for MOFMs applied to separate  $CO_2/O_2$  gas pair mainly is approximately 2.5–7.5 Å and the optimal PLD range for MOFMs applied to separate  $CO_2/N_2$  gas pair is approximately 2–5 Å.

### 3.3. Separation of $CO_2/N_2/O_2$ Pairs

In this work, the vol% of  $CO_2/N_2/O_2$  pairs at 298 K and 1 bar is 1:1:1. For the purpose of  $CO_2$  capture instead of  $O_2$  and  $N_2$ , it is essential use MOFMs with a large  $P_{CO_2}$ , a small  $P_{N_2}$  and a small  $P_{O_2}$  even under large permselectivity. As such, 44 MOFMs used to separate  $CO_2/O_2$  and 38 MOFMs used to separate  $CO_2/N_2$  were, respectively, screened under the condition of  $P_{CO_2} \geq 10^6$  barrer and  $S_{perm} \geq 10^6$  at first, as shown in the red area of Figure 3a,b. Of the above MOFMs, there are approximately 91% LCD of MOFMs for  $CO_2/O_2$  separation under the optimal LCD range and approximately 84% PLD of MOFMs for  $CO_2/N_2$  separation under the optimal PLD range, which demonstrates the effectiveness of ML analysis. Furthermore, in the search for promising MOFMs for practical application, seven top-performing MOFMs with  $P_{N_2}$  and  $P_{O_2}$  less than 100 barrer were selected, with structural characteristics found to completely follow the optimal LCD and PLD range. The details of seven top-performing MOFMs are listed in Table S10. Due to the similar atomistic structures of three MOFMs, the seven top-performing MOFMs are shown divided in Figures 5 and S15.

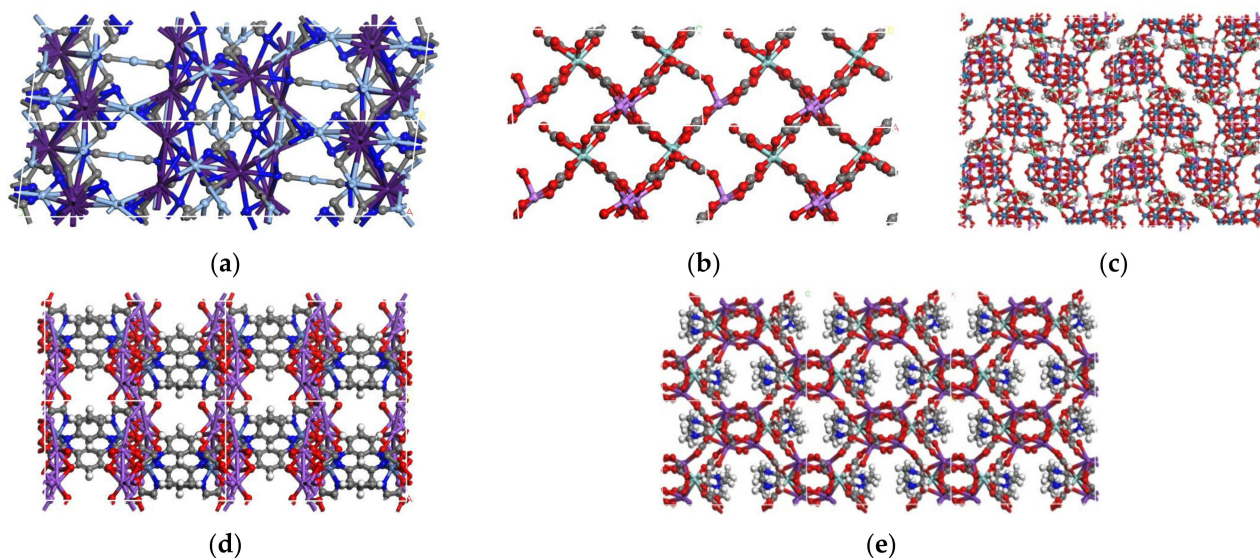


**Figure 5.** Atomistic structures of top-performing MOFMs. (a) CARGEI; (b) YUJWAD; (c) RIPWEU; (d) VEHNED; (e) WOCJII.

Moreover, the ranges of other structural descriptors were analyzed. The VSA of the majority of MOFMs is smaller than  $140 \text{ m}^2/\text{cm}^3$  and approximately 60% have a VSA smaller than  $30 \text{ m}^2/\text{cm}^3$ . The  $\phi$  of the MOFMs is not greater than 0.3. The  $\rho$  of 71% of MOFMs is not larger than  $1600 \text{ kg}/\text{m}^3$ . Further, the  $PSD\%_{(2.5-3.5)}$  of 86% of MOFMs is less than 4%. The above conclusions on the range of optimal potential MOFMs once more demonstrates the importance of available permeance area for the permeance performance of gas molecules with smaller kinetic diameters.



#### 4. Conclusions

In this work, the permeability of pure CO<sub>2</sub>, N<sub>2</sub>, and O<sub>2</sub> in CoRE-MOFMs was calculated by GCMC and MD simulations to select MOFMs for the purification of flue gas. Univariate analysis showed the great impact of available permeance area to the permeance performance of gas molecules with smaller kinetic diameters. Further, the adsorption mechanism has a dominant role in the membrane separation mechanism for both CO<sub>2</sub>/N<sub>2</sub> and CO<sub>2</sub>/O<sub>2</sub> gas pairs. Furthermore, to comprehensively understand the order of importance of structural descriptors to permeance performance, seven classification algorithms were applied to predict categories of permeance performance, from which XGBoost was selected due to optimal prediction accuracy. Through ML calculations, the impact of available permeance area was demonstrated one more time. LCD and PLD were found to significantly impact the separation of CO<sub>2</sub>/O<sub>2</sub> and CO<sub>2</sub>/N<sub>2</sub>, respectively. Finally, considering the purpose of CO<sub>2</sub> capture, seven promising MOFMs with optimal permeance performance were screened. Their LCD and PLD completely conformed to the optimal LCD and PLD ranges by mining big data and ML, respectively. After the analysis of other structural descriptor ranges, the importance of available permeance area to permeance performance was illustrated for membrane separation by MOFMs. This work can provide explicit directions and powerful guidelines to study the capture of CO<sub>2</sub> in flue gas by membrane separation.

**Supplementary Materials:** The following supporting information can be downloaded at: <https://www.mdpi.com/article/10.3390/membranes12070700/s1>, Figure S1:  $P_{N_2}/P_{O_2}/S_{perm} (CO_2/O_2)$ -PLD,  $\phi$ , VSA, and  $\rho$ ; Figure S2: (a) LCD- $P_{CO_2}$ - $S_{perm} (CO_2/N_2)$ ; (b) PLD- $P_{CO_2}$ - $S_{perm} (CO_2/O_2)$ ; (c)  $P_{N_2}$ -LCD; (d)  $P_{O_2}$ -LCD; (e) D-PLD; Figure S3:  $P/S_{perm}$ -PSD%<sub>(2.5-3.5)</sub>. Figure S4: The calculation schematic diagram for the accuracy, sensitive, and specificity; Figure S5: The accuracy, sensitive, and specificity comparison of seven algorithms for  $S_{perm} (CO_2/N_2)$  and  $S_{perm} (CO_2/O_2)$ ; Figure S6: The diagram of  $k$ -fold cross validation; Figure S7: KNN algorithm model; Figure S8: SVM algorithm model; Figure S9: DT algorithm model; Figure S10: RF algorithm model; Figure S11: GBDT algorithm model; Figure S12: The leaf-wise tree growth schematic diagram of LGBM algorithm model; Figure S13: XGBoost algorithm model; Figure S14: Confusion matrix from best model; Figure S15: Atomistic structures of top-performance MOFMs. Table S1: Lennard–Jones parameters of metal–organic frameworks (MOFs); Table S2: Lennard–Jones parameters and charges of adsorbates; Table S3: Optimal hyperparameters for SVM, KNN, DT, RF, and GBDT; Table S4: Optimal hyperparameters for LGBM and XGBoost; Table S5: Evaluation of seven ML algorithm for  $P$ ; Table S6: Evaluation of seven ML algorithm for  $S_{perm}$ ; Table S7: Evaluation of XGBoost for  $P_{CO_2}$  and  $P_{O_2}$ ; Table S8: Evaluation of XGBoost for  $P_{N_2}$ ; Table S9: Evaluation of XGBoost for  $S_{perm} (CO_2/O_2)$  and  $S_{perm} (CO_2/N_2)$ ; Table S10: Seven top-performance MOFMs for CO<sub>2</sub>/N<sub>2</sub>/O<sub>2</sub> separation [9,37,53–61].

**Author Contributions:** Conceptualization, Z.Q., X.Z. and B.W.; methodology, Z.Q., B.W. and Y.S.; software, Z.Q., H.L. and S.L.; validation, Y.S., X.Y. and X.B.; formal analysis, X.Y. and X.B.; investigation, X.Z.; resources, Z.Q.; data curation, Z.Q.; writing—original draft preparation, Y.S., B.W. and Z.Q.; writing—review and editing, X.Z., B.W. and Z.Q.; visualization, Y.S.; supervision, X.Z.; project administration, B.W.; funding acquisition, Z.Q. All authors have read and agreed to the published version of the manuscript.

**Funding:** This research was funded by the National Natural Science Foundation of China (21978058 and 21676094), the Pearl River Talent Recruitment Program (2019QN01L255), the Natural Science Foundation of Guangdong Province (2022A1515011446 and 2020A1515010800), the Guangzhou Municipal Science and Technology Project (202102020875) and the R & D Program of the Joint Institute of GZHU and ICoST (GI202102).

**Institutional Review Board Statement:** “Not applicable” for studies not involving humans or animals.

**Informed Consent Statement:** Not applicable.

**Data Availability Statement:** Data is contained within the article or Supplementary Material.

**Acknowledgments:** We gratefully thank the National Natural Science Foundation of China (21978058 and 21676094), the Pearl River Talent Recruitment Program (2019QN01L255), the Natural Science Foundation of Guangdong Province (2022A1515011446 and 2020A1515010800), the Guangzhou Municipal Science and Technology Project (202102020875) and the R & D Program of the Joint Institute of GZHU and ICoST (GI202102) for financial support.

**Conflicts of Interest:** The authors declare no conflict of interest.

## References

1. Yagihara, K.; Ohno, H.; Guzman-Urbina, A.; Ni, J.; Fukushima, Y. Analyzing flue gas properties emitted from power and industrial sectors toward heat-integrated carbon capture. *Energy* **2022**, *250*, 123775. [\[CrossRef\]](#)
2. Qian, Q.; Asinger, P.A.; Lee, M.J.; Han, G.; Mizrahi Rodriguez, K.; Lin, S.; Benedetti, F.M.; Wu, A.X.; Chi, W.S.; Smith, Z.P. MOF-Based Membranes for Gas Separations. *Chem. Rev.* **2020**, *120*, 8161–8266. [\[CrossRef\]](#)
3. Liu, X.; Liang, T.; Zhang, R.; Ding, Q.; Wu, S.; Li, C.; Lin, Y.; Ye, Y.; Zhong, Z.; Zhou, M. Iron-Based Metal-Organic Frameworks in Drug Delivery and Biomedicine. *ACS Appl. Mater. Interfaces* **2021**, *13*, 9643–9655. [\[CrossRef\]](#)
4. Guo, M.; Zhang, M.; Liu, R.; Zhang, X.; Li, G. State-of-the-Art Advancements in Photocatalytic Hydrogenation: Reaction Mechanism and Recent Progress in Metal-Organic Framework (MOF)-Based Catalysts. *Adv. Sci.* **2022**, *9*, e2103361. [\[CrossRef\]](#)
5. Lim, D.W.; Chyun, S.A.; Suh, M.P. Hydrogen storage in a potassium-ion-bound metal-organic framework incorporating crown ether struts as specific cation binding sites. *Angew. Chem.-Int. Edit.* **2014**, *53*, 7819–7822. [\[CrossRef\]](#) [\[PubMed\]](#)
6. Mason, J.A.; Oktawiec, J.; Taylor, M.K.; Hudson, M.R.; Rodriguez, J.; Bachman, J.E.; Gonzalez, M.I.; Cervellino, A.; Guagliardi, A.; Brown, C.M.; et al. Methane storage in flexible metal-organic frameworks with intrinsic thermal management. *Nature* **2015**, *527*, 357–361. [\[CrossRef\]](#) [\[PubMed\]](#)
7. Prasetyo, N.; Pambudi, F.I. Toward hydrogen storage material in fluorinated zirconium metal-organic framework (MOF-801): A periodic density functional theory (DFT) study of fluorination and adsorption. *Int. J. Hydrog. Energy* **2021**, *46*, 4222–4228. [\[CrossRef\]](#)
8. Shi, Z.; Yang, W.; Deng, X.; Cai, C.; Yan, Y.; Liang, H.; Liu, Z.; Qiao, Z. Machine-learning-assisted high-throughput computational screening of high performance metal-organic frameworks. *Mol. Syst. Des. Eng.* **2020**, *5*, 725–742. [\[CrossRef\]](#)
9. Qiao, Z.; Li, L.; Li, S.; Liang, H.; Zhou, J.; Snurr, R.Q. Molecular fingerprint and machine learning to accelerate design of high-performance homochiral metal-organic frameworks. *AIChE J.* **2021**, *67*, e17352. [\[CrossRef\]](#)
10. Yuan, X.; Deng, X.; Cai, C.; Shi, Z.; Liang, H.; Li, S.; Qiao, Z. Machine learning and high-throughput computational screening of hydrophobic metal-organic frameworks for capture of formaldehyde from air. *Green Energy Environ.* **2021**, *6*, 759–770. [\[CrossRef\]](#)
11. Yuan, X.; Li, L.; Shi, Z.; Liang, H.; Li, S.; Qiao, Z. Molecular-fingerprint machine-learning-assisted design and prediction for high-performance MOFs for capture of NMHCs from air. *Adv. Powder Mater.* **2022**, *1*, 100026. [\[CrossRef\]](#)
12. McDonald, T.M.; Mason, J.A.; Kong, X.; Bloch, E.D.; Gygi, D.; Dani, A.; Crocella, V.; Giordanino, F.; Odoh, S.O.; Drisdell, W.S.; et al. Cooperative insertion of CO<sub>2</sub> in diamine-appended metal-organic frameworks. *Nature* **2015**, *519*, 303–308. [\[CrossRef\]](#)
13. Li, J.R.; Yu, J.; Lu, W.; Sun, L.B.; Sculley, J.; Balbuena, P.B.; Zhou, H.C. Porous materials with pre-designed single-molecule traps for CO<sub>2</sub> selective adsorption. *Nat. Commun.* **2013**, *4*, 1538. [\[CrossRef\]](#)
14. Zhang, X.; Lin, R.B.; Wang, J.; Wang, B.; Liang, B.; Yildirim, T.; Zhang, J.; Zhou, W.; Chen, B. Optimization of the Pore Structures of MOFs for Record High Hydrogen Volumetric Working Capacity. *Adv. Mater.* **2020**, *32*, e1907995. [\[CrossRef\]](#)
15. Zhang, X.; Lin, R.-B.; Wu, H.; Huang, Y.; Ye, Y.; Duan, J.; Zhou, W.; Li, J.-R.; Chen, B. Maximizing acetylene packing density for highly efficient C<sub>2</sub>H<sub>2</sub>/CO<sub>2</sub> separation through immobilization of amine sites within a prototype MOF. *Chem. Eng. J.* **2022**, *431*, 134184. [\[CrossRef\]](#)
16. Boyd, P.G.; Chidambaram, A.; Garcia-Diez, E.; Ireland, C.P.; Daff, T.D.; Bounds, R.; Gladysiak, A.; Schouwink, P.; Moosavi, S.M.; Maroto-Valer, M.M.; et al. Data-driven design of metal-organic frameworks for wet flue gas CO<sub>2</sub> capture. *Nature* **2019**, *576*, 253–256. [\[CrossRef\]](#)
17. Nugent, P.; Belmabkhout, Y.; Burd, S.D.; Cairns, A.J.; Luebke, R.; Forrest, K.; Pham, T.; Ma, S.; Space, B.; Wojtas, L.; et al. Porous materials with optimal adsorption thermodynamics and kinetics for CO<sub>2</sub> separation. *Nature* **2013**, *495*, 80–84. [\[CrossRef\]](#)
18. Yin, H.; Wang, J.; Xie, Z.; Yang, J.; Bai, J.; Lu, J.; Zhang, Y.; Yin, D.; Lin, J.Y. A highly permeable and selective amino-functionalized MOF CAU-1 membrane for CO<sub>2</sub>-N<sub>2</sub> separation. *Chem. Commun.* **2014**, *50*, 3699–3701. [\[CrossRef\]](#)
19. Chang, H.; Wang, Y.; Xiang, L.; Liu, D.; Wang, C.; Pan, Y. Improved H<sub>2</sub>/CO<sub>2</sub> separation performance on mixed-linker ZIF-7 polycrystalline membranes. *Chem. Eng. Sci.* **2018**, *192*, 85–93. [\[CrossRef\]](#)
20. Kang, Z.; Fan, L.; Wang, S.; Sun, D.; Xue, M.; Qiu, S. In situ confinement of free linkers within a stable MOF membrane for highly improved gas separation properties. *CrystEngComm* **2017**, *19*, 1601–1606. [\[CrossRef\]](#)
21. Fan, S.T.; Qiu, Z.J.; Xu, R.Y.; Zhang, S.X.; Chen, Z.H.; Nie, Z.J.; Shu, H.R.; Guo, K.; Zhang, S.; Li, B.J. Ultrahigh Carbon Dioxide-Selective Composite Membrane Containing a gamma-CD-MOF Layer. *ACS Appl. Mater. Interfaces* **2021**, *13*, 13034–13043. [\[CrossRef\]](#)
22. Yan, J.; Sun, Y.; Ji, T.; Zhang, C.; Liu, L.; Liu, Y. Room-temperature synthesis of defect-engineered Zirconium-MOF membrane enabling superior CO<sub>2</sub>/N<sub>2</sub> selectivity with zirconium-oxo cluster source. *J. Membr. Sci.* **2022**, *653*, 120496. [\[CrossRef\]](#)

23. Chen, S.S.; Yang, Z.-J.; Chang, C.-H.; Koh, H.-U.; Al-Saeedi, S.I.; Tung, K.-L.; Wu, K.C.W. Interfacial nanoarchitectonics for ZIF-8 membranes with enhanced gas separation. *Beilstein J. Nanotechnol.* **2022**, *13*, 313–324. [[CrossRef](#)]
24. Qiao, Z.; Peng, C.; Zhou, J.; Jiang, J. High-throughput computational screening of 137953 metal–organic frameworks for membrane separation of a CO<sub>2</sub>/N<sub>2</sub>/CH<sub>4</sub> mixture. *J. Mater. Chem. A* **2016**, *4*, 15904–15912. [[CrossRef](#)]
25. Glover, J.; Besley, E. A high-throughput screening of metal-organic framework based membranes for biogas upgrading. *Faraday Discuss.* **2021**, *231*, 235–257. [[CrossRef](#)]
26. Azar, A.N.V.; Velioglu, S.; Keskin, S. Large-Scale Computational Screening of Metal Organic Framework (MOF) Membranes and MOF-Based Polymer Membranes for H<sub>2</sub>/N<sub>2</sub> Separations. *ACS Sustain. Chem. Eng.* **2019**, *7*, 9525–9536. [[CrossRef](#)]
27. Daglar, H.; Keskin, S. Computational Screening of Metal–Organic Frameworks for Membrane-Based CO<sub>2</sub>/N<sub>2</sub>/H<sub>2</sub>O Separations: Best Materials for Flue Gas Separation. *J. Phys. Chem. C* **2018**, *122*, 17347–17357. [[CrossRef](#)]
28. Altintas, C.; Keskin, S. Molecular simulations of MOF membranes for separation of ethane/ethene and ethane/methane mixtures. *RSC Adv.* **2017**, *7*, 52283–52295. [[CrossRef](#)] [[PubMed](#)]
29. Wang, F.; Sose, A.T.; Singh, S.K.; Deshmukh, S.A. Dual-Force Zone Nonequilibrium Molecular Dynamics Simulations on Nanoporous Metal–Organic Framework Membranes for Separation of H<sub>2</sub>/CH<sub>4</sub> Mixtures. *ACS Appl. Nano Mater.* **2022**, *5*, 4048–4061. [[CrossRef](#)]
30. Bai, X.; Shi, Z.; Xia, H.; Li, S.; Liu, Z.; Liang, H.; Liu, Z.; Wang, B.; Qiao, Z. Machine-Learning-Assisted High-Throughput computational screening of Metal–Organic framework membranes for hydrogen separation. *Chem. Eng. J.* **2022**, *446*, 136783. [[CrossRef](#)]
31. Su, Y.; Zhang, S.; Liu, L.; Xu, D.; Xiong, Y. Investigation of representative components of flue gas used as torrefaction pretreatment atmosphere and its effects on fast pyrolysis behaviors. *Bioresour. Technol.* **2018**, *267*, 584–590. [[CrossRef](#)]
32. He, X.; Hägg, M.-B. Structural, kinetic and performance characterization of hollow fiber carbon membranes. *J. Membr. Sci.* **2012**, *390*, 23–31. [[CrossRef](#)]
33. Mabuza, M.; Premllall, K.; Onyango, M.; Daramola, M.O. Low-high temperature flue gas direct injection in south African bituminous and anthracite coals: Sorption capacity assessment. *Curr. Sci.* **2018**, *115*, 682–691. [[CrossRef](#)]
34. Chung, Y.G.; Haldoupis, E.; Bucior, B.J.; Haranczyk, M.; Lee, S.; Zhang, H.; Vogiatzis, K.D.; Milisavljevic, M.; Ling, S.; Camp, J.S.; et al. Advances, Updates, and Analytics for the Computation-Ready, Experimental Metal–Organic Framework Database: CoRE MOF 2019. *J. Chem. Eng. Data* **2019**, *64*, 5985–5998. [[CrossRef](#)]
35. Chung, Y.G.; Camp, J.; Haranczyk, M.; Sikora, B.J.; Bury, W.; Krungleviciute, V.; Yildirim, T.; Farha, O.K.; Sholl, D.S.; Snurr, R.Q. Computation-Ready, Experimental Metal–Organic Frameworks: A Tool to Enable High-Throughput Screening of Nanoporous Crystals. *Chem. Mater.* **2014**, *26*, 6185–6192. [[CrossRef](#)]
36. Kadantsev, E.S.; Boyd, P.G.; Daff, T.D.; Woo, T.K. Fast and Accurate Electrostatics in Metal Organic Frameworks with a Robust Charge Equilibration Parameterization for High-Throughput Virtual Screening of Gas Adsorption. *J. Phys. Chem. Lett.* **2013**, *4*, 3056–3061. [[CrossRef](#)]
37. Rappe, A.K.; Casewit, C.J.; Colwell, K.S.; Goddard, W.A.; Skiff, W.M. UFF A Full Periodic Table Force Field for Molecular Mechanics and Molecular Dynamics Simulation. *J. Am. Chem. Soc.* **1992**, *114*, 10024–10035. [[CrossRef](#)]
38. Dubbeldam, D.; Calero, S.; Ellis, D.E.; Snurr, R.Q. RASPA: Molecular simulation software for adsorption and diffusion in flexible nanoporous materials. *Mol. Simul.* **2016**, *42*, 81–101. [[CrossRef](#)]
39. Willems, T.F.; Rycroft, C.H.; Kazi, M.; Meza, J.C.; Haranczyk, M. Algorithms and tools for high-throughput geometry-based analysis of crystalline porous materials. *Microporous Mesoporous Mater.* **2012**, *149*, 134–141. [[CrossRef](#)]
40. Potoff, J.J.; Siepmann, J.I. Vapor-liquid equilibria of mixtures containing alkanes, carbon dioxide, and nitrogen. *AIChE J.* **2001**, *47*, 1676–1682. [[CrossRef](#)]
41. Shi, Z.; Liang, H.; Yang, W.; Liu, J.; Liu, Z.; Qiao, Z. Machine learning and in silico discovery of metal-organic frameworks: Methanol as a working fluid in adsorption-driven heat pumps and chillers. *Chem. Eng. Sci.* **2020**, *214*, 115430. [[CrossRef](#)]
42. Shi, Z.; Yuan, X.; Yan, Y.; Tang, Y.; Li, J.; Liang, H.; Tong, L.; Qiao, Z. Techno-economic analysis of metal–organic frameworks for adsorption heat pumps/chillers: From directional computational screening, machine learning to experiment. *J. Mater. Chem. A* **2021**, *9*, 7656–7666. [[CrossRef](#)]
43. Park, J.; Suh, B.L.; Kim, J. Computational Design of a Photoresponsive Metal–Organic Framework for Post Combustion Carbon Capture. *J. Phys. Chem. C* **2020**, *124*, 13162–13167. [[CrossRef](#)]
44. Yan, Y.; Shi, Z.; Li, H.; Li, L.; Yang, X.; Li, S.; Liang, H.; Qiao, Z. Machine learning and in-silico screening of metal–organic frameworks for O<sub>2</sub>/N<sub>2</sub> dynamic adsorption and separation. *Chem. Eng. J.* **2022**, *427*, 131604. [[CrossRef](#)]
45. Ewald, P.P. Die Berechnung optischer und elektrostatischer Gitterpotentiale. *Ann. Phys.* **1921**, *369*, 253–287. [[CrossRef](#)]
46. Robeson, L.M. The upper bound revisited. *J. Membr. Sci.* **2008**, *320*, 390–400. [[CrossRef](#)]
47. Watanabe, T.; Manz, T.A.; Sholl, D.S. Accurate Treatment of Electrostatics during Molecular Adsorption in Nanoporous Crystals without Assigning Point Charges to Framework Atoms. *J. Phys. Chem. C* **2011**, *115*, 4824–4836. [[CrossRef](#)]
48. Haldoupis, E.; Nair, S.; Sholl, D.S. Finding MOFs for highly selective CO<sub>2</sub>/N<sub>2</sub> adsorption using materials screening based on efficient assignment of atomic point charges. *J. Am. Chem. Soc.* **2012**, *134*, 4313–4323. [[CrossRef](#)]
49. Watanabe, T.; Sholl, D.S. Accelerating applications of metal-organic frameworks for gas adsorption and separation by computational screening of materials. *Langmuir* **2012**, *28*, 14114–14128. [[CrossRef](#)]

50. Altintas, C.; Keskin, S. Role of partial charge assignment methods in high-throughput screening of MOF adsorbents and membranes for CO<sub>2</sub>/CH<sub>4</sub> separation. *Mol. Syst. Des. Eng.* **2020**, *5*, 532–543. [[CrossRef](#)]
51. Wang, J.; Zhou, M.; Lu, D.; Fei, W.; Wu, J. Computational screening and design of nanoporous membranes for efficient carbon isotope separation. *Green Energy Environ.* **2020**, *5*, 364–373. [[CrossRef](#)]
52. Zhou, M.; Vassallo, A.; Wu, J. Toward the inverse design of MOF membranes for efficient D<sub>2</sub>/H<sub>2</sub> separation by combination of physics-based and data-driven modeling. *J. Membr. Sci.* **2020**, *598*, 117675. [[CrossRef](#)]
53. Shah, M.S.; Tsapatsis, M.; Siepmann, J.I. Development of the Transferable Potentials for Phase Equilibria Model for Hydrogen Sulfide. *J. Phys. Chem. B* **2015**, *119*, 7041–7052. [[CrossRef](#)] [[PubMed](#)]
54. Pedregosa, F.; Varoquaux, G.; Gramfort, A.; Michel, V.; Thirion, B.; Grisel, O.; Blondel, M.; Prettenhofer, P.; Weiss, R.; Dubourg, V.; et al. Scikit-learn: Machine Learning in Python. *J. Mach. Learn. Res.* **2011**, *12*, 2825–2830.
55. Available online: <http://scikit-optimize.github.io/stable/modules/bayessearchcv.html> (accessed on 8 June 2022).
56. Cover, T.M.; Hart, P.E. Nearest Neighbor Pattern Classification. *IEEE Trans. Inf. Theory* **1967**, *13*, 21. [[CrossRef](#)]
57. Scholkopf, B.; Sung, K.-K.; Burges, C.J.C.; Girosi, F.; Niyogi, P.; Poggio, T.; Vapnik, V.; Tran, I. Comparing Support Vector Machines with Gaussian Kernels to Radial Basis Function Classifiers. *IEEE Trans. Signal Process.* **1997**, *45*, 2758–2765. [[CrossRef](#)]
58. Yin, F.; Shao, X.; Zhao, L.; Li, X.; Zhou, J.; Cheng, Y.; He, X.; Lei, S.; Li, J.; Wang, J. Predicting prognosis of endometrioid endometrial adenocarcinoma on the basis of gene expression and clinical features using Random Forest. *Oncol. Lett.* **2019**, *18*, 1597–1606. [[CrossRef](#)]
59. Friedman, J.H. Greedy function approximation: A gradient boosting machine. *Ann. Stat.* **2001**, *29*, 1189–1232. [[CrossRef](#)]
60. Available online: <https://lightgbm.readthedocs.io/en/latest/Features.html> (accessed on 8 June 2022).
61. Available online: <https://xgboost.readthedocs.io/en/stable/> (accessed on 8 June 2022).